

## Supplementary Information

### **Achieving a 2.7 V aqueous hybrid supercapacitor by the pH- regulation of electrolyte**

Lijun Su,<sup>a,b</sup> Qingnuan Zhang,<sup>a</sup> Yue Wang,<sup>c</sup> Jianing Meng,<sup>c</sup> Yongtai Xu,<sup>a,b</sup> Lingyang  
Liu,<sup>a,b</sup> and Xingbin Yan<sup>\*a,b,d</sup>

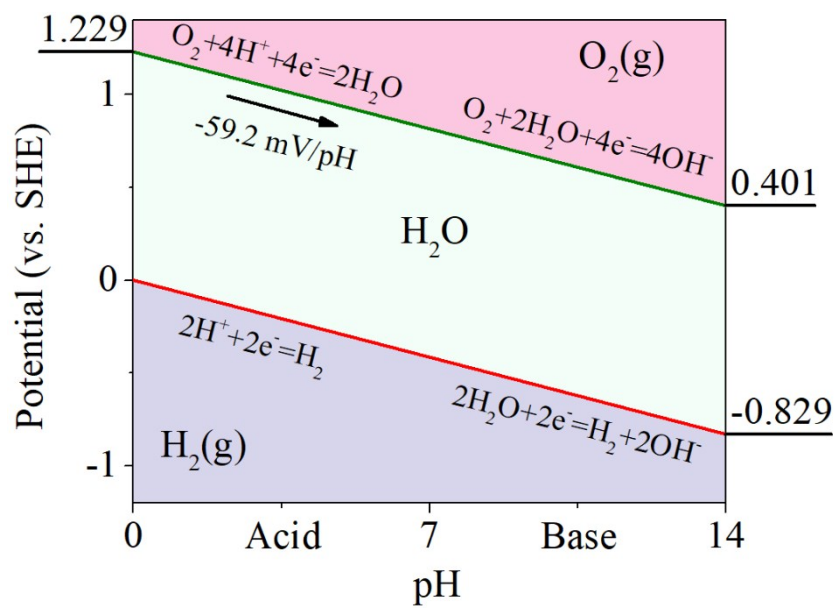
<sup>a</sup> Laboratory of Clean Energy Chemistry and Materials, State Key Laboratory of Solid Lubrication, Lanzhou Institute of Chemical Physics, Chinese Academy of Sciences, Lanzhou 730000, P.R. China.

<sup>b</sup> Center of Materials Science and Optoelectronics Engineering, University of Chinese Academy of Sciences, Beijing 100049, P.R. China.

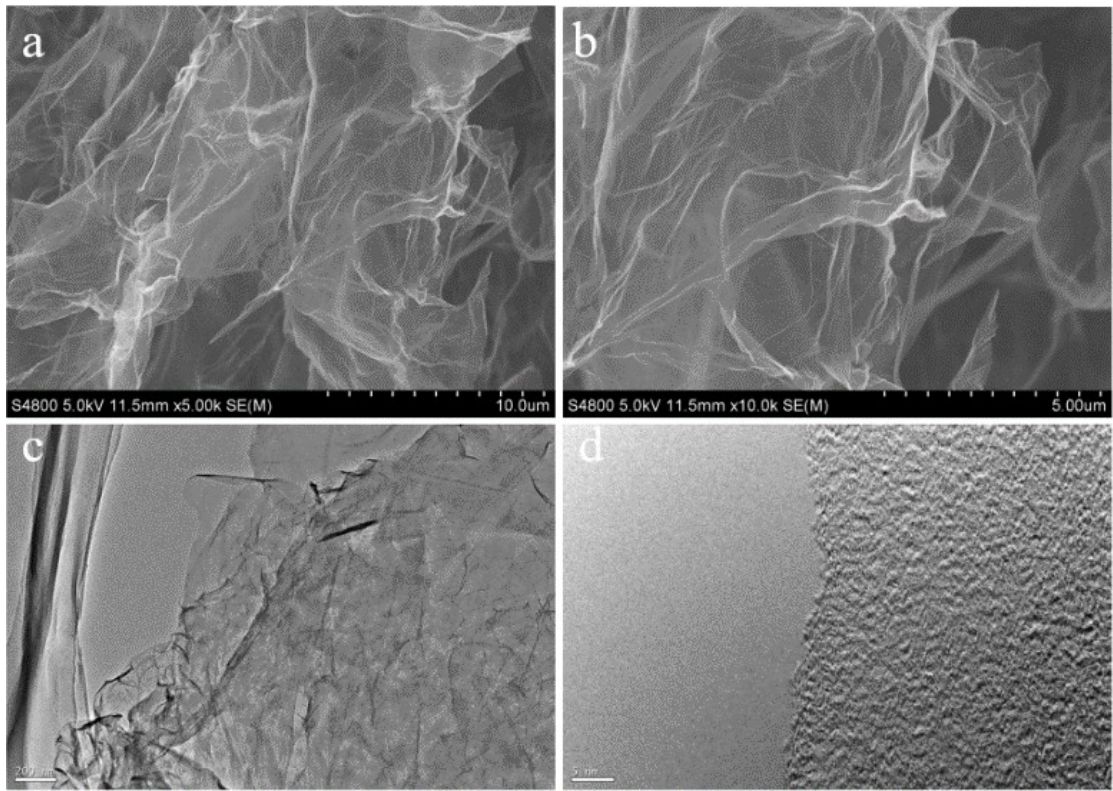
<sup>c</sup> School of Physical Science and Technology, Lanzhou University, Lanzhou, 730000, P.R. China.

<sup>d</sup> Dalian National Laboratory for Clean Energy, Dalian 116023, P.R. China.

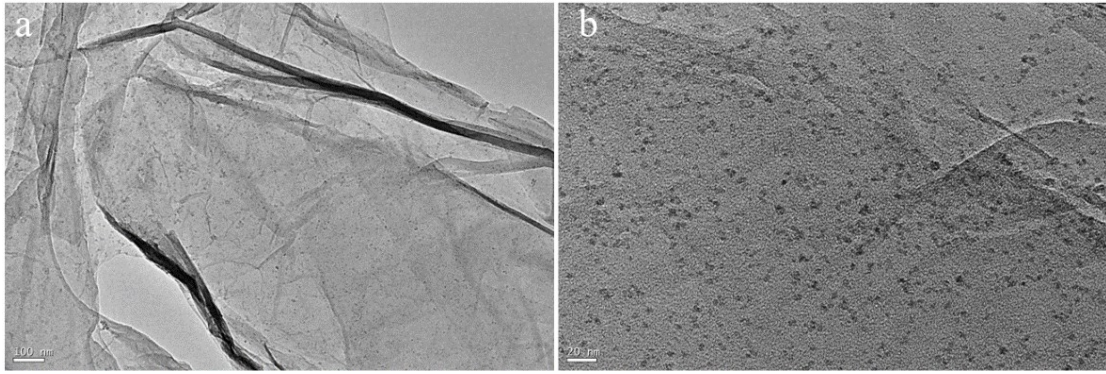
\*Corresponding author: XingBin Yan (email: xbyan@licp.cas.cn)



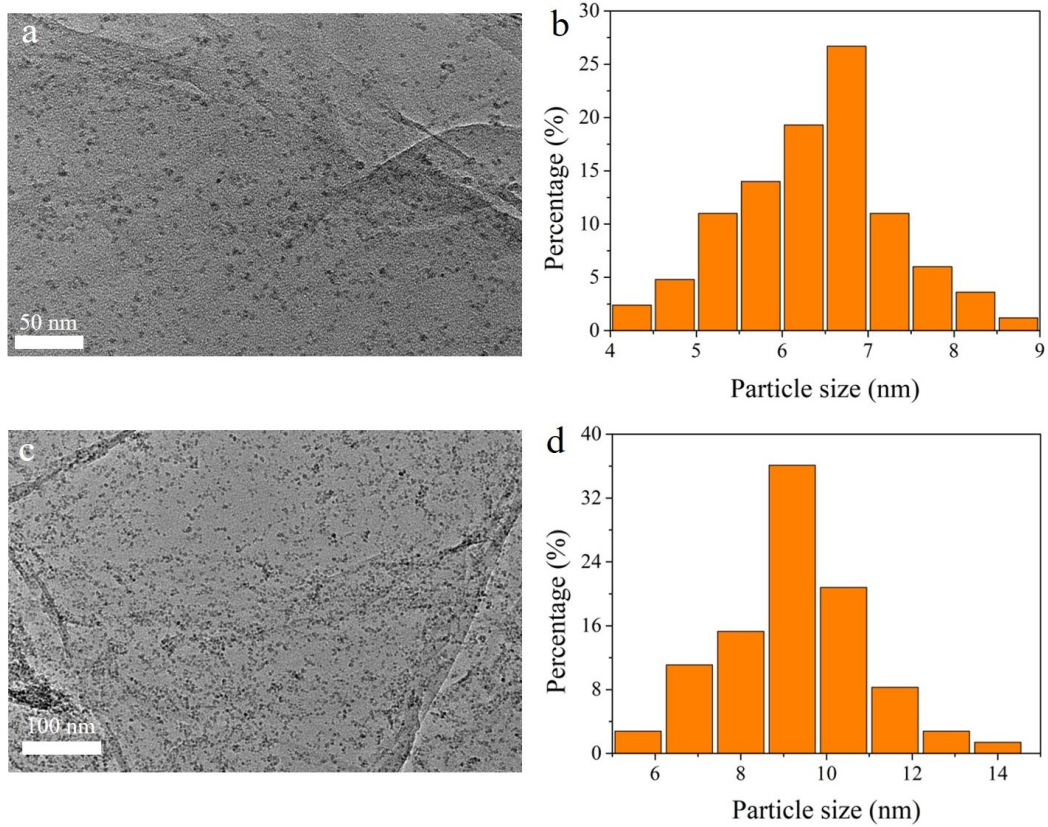
**Figure S1.** Electrochemical stable window of aqueous electrolytes at a constant of 1.23 V as governed by Pourbaix diagram.<sup>1</sup>



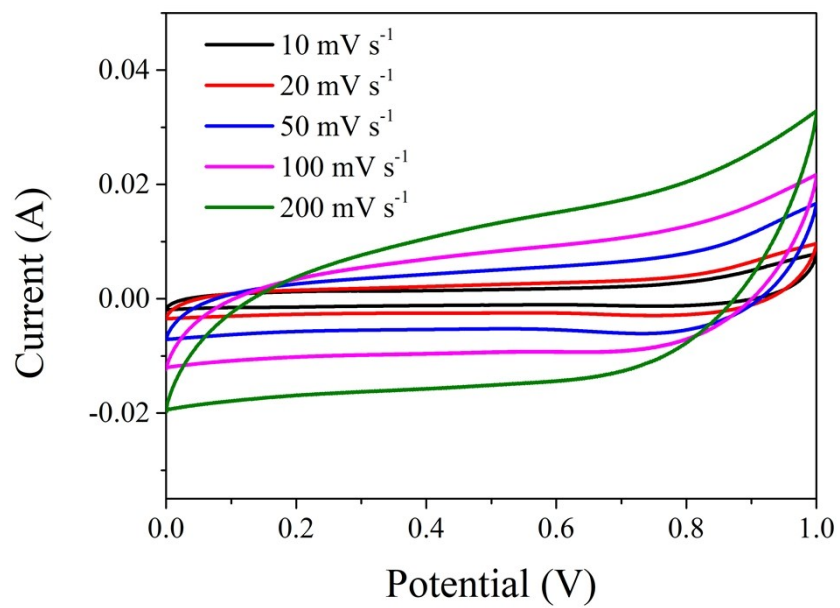
**Figure S2.** SEM images of pure graphene after the first-step solvothermal reaction with scale size of 10  $\mu\text{m}$  (a) and 5  $\mu\text{m}$  (b). TEM images of graphene with scale size of 20 nm (c) and 5 nm (d).



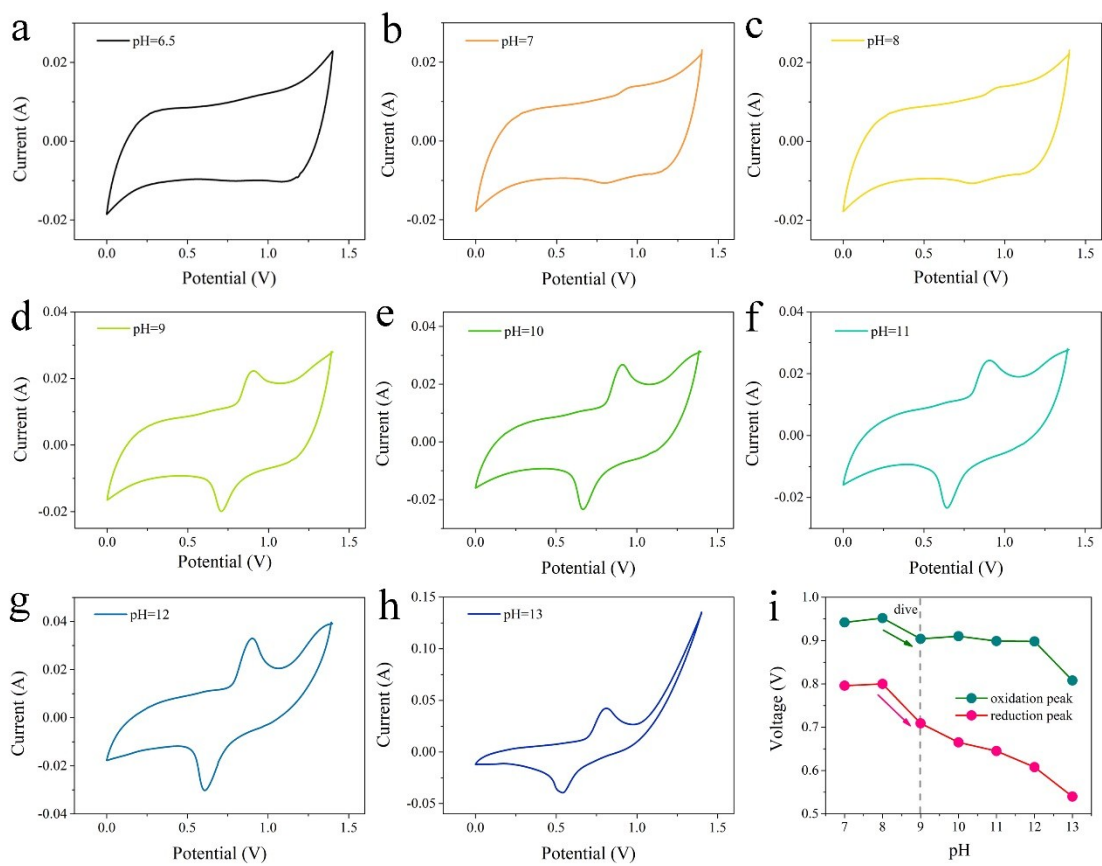
**Figure S3.** TEM images of  $\text{Mn}_3\text{O}_4$  nanodots anchored on graphene with scale size of 100 nm (a) and 20 nm (b).



**Figure S4.** TEM images of Mn<sub>3</sub>O<sub>4</sub>-NDs@NG (a, scale bar is 50 nm) and NMO-NDs@NG (c, scale bar is 100 nm). The statistical size distribution of Mn<sub>3</sub>O<sub>4</sub>-NDs (b) and NMO-NDs (d) by nano measurer software.

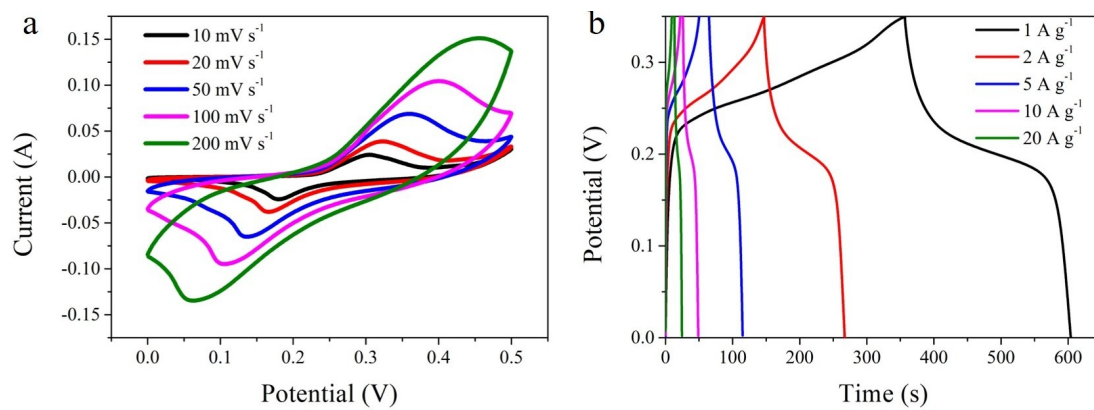


**Figure S5.** The electrochemical performance of NG in Na<sub>2</sub>SO<sub>4</sub> electrolyte. CV curves from 10 to 200 mV s<sup>-1</sup>.



**Figure S6.** (a-h) CV curves of NMO-NDs@NG electrode at the electrolytes with the pH values ranging from 6.5 to 13. (i) The potential position of redox peaks varies with the pH value.

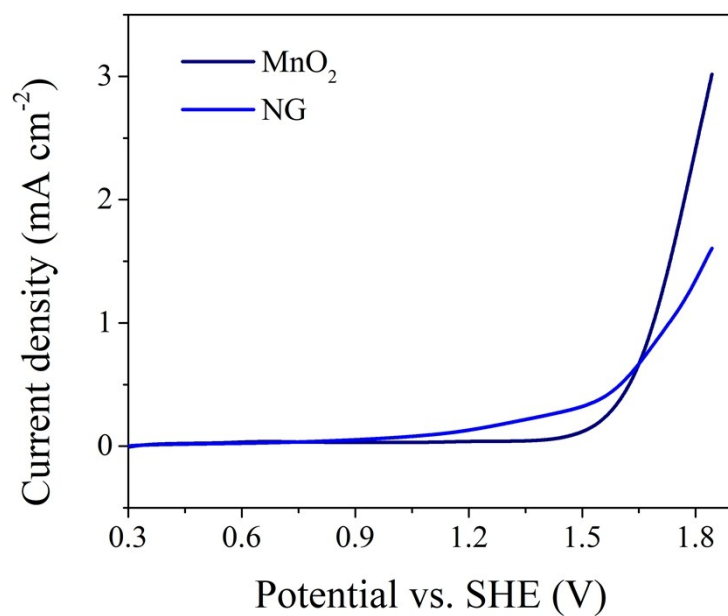




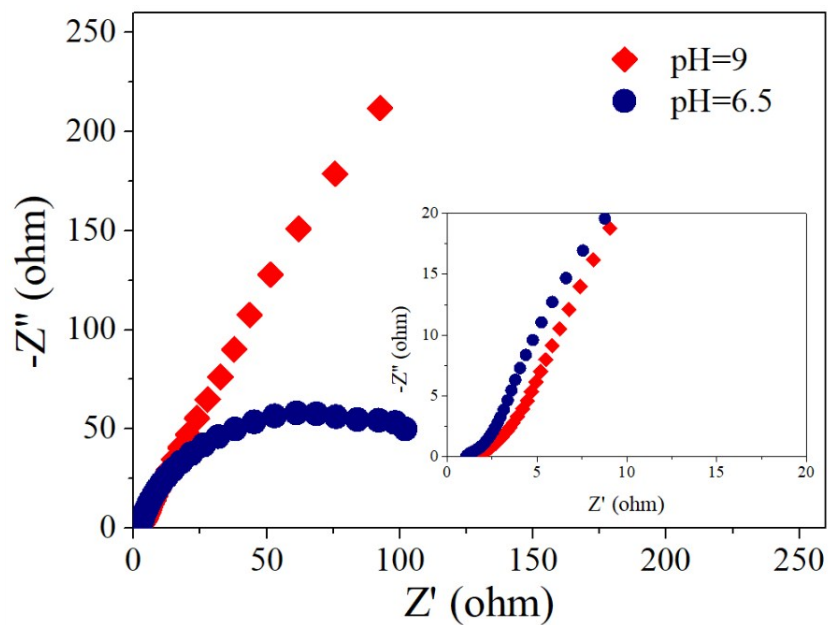
**Figure S7.** The electrochemical performance of NMO-NDs@NG in KOH electrolyte.

(a) CV curves from 10 to 200 mV s<sup>-1</sup>, (b) GCD plots from 1 to 20 A g<sup>-1</sup>.

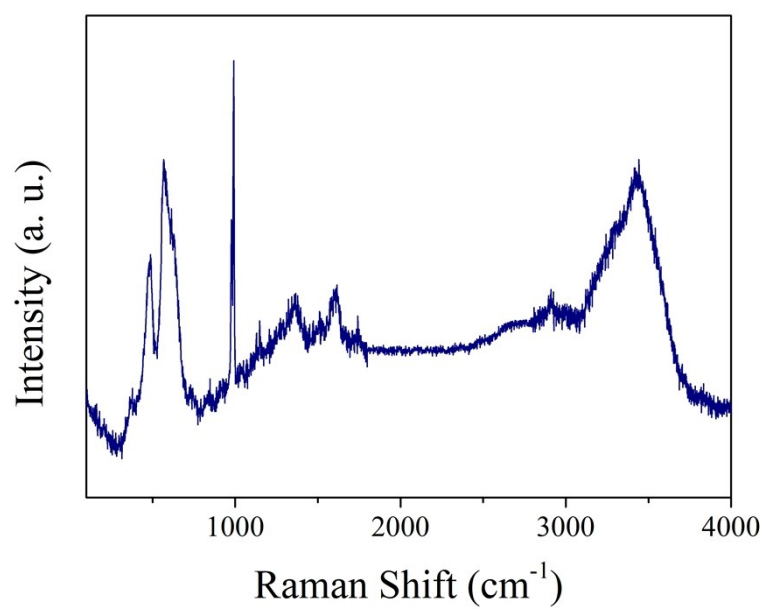




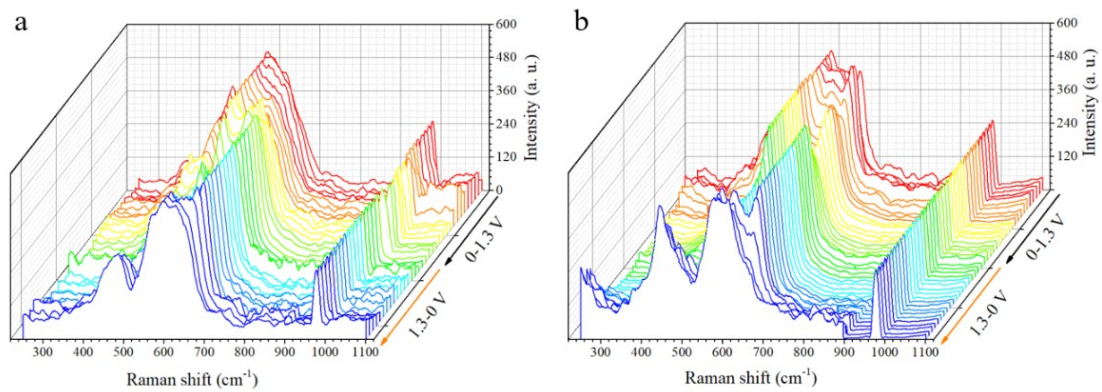
**Figure S8.** Linear sweep voltammetry (LSV) curves of MnO<sub>2</sub> and NG in Na<sub>2</sub>SO<sub>4</sub>-based electrolytes of pH=9 under the three-electrode system and at the scan rate of 10 mV s<sup>-1</sup>.



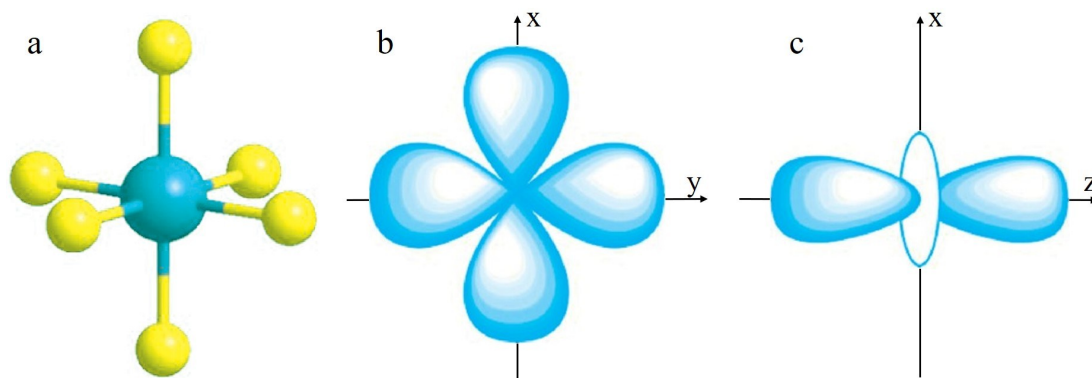
**Figure S9.** The electrochemical impedance spectrum of NMO-NDs@NG at 1.3 V in the electrolytes with pH=6.5 and pH=9. Inset is the enlarged diagram at the high frequency region.



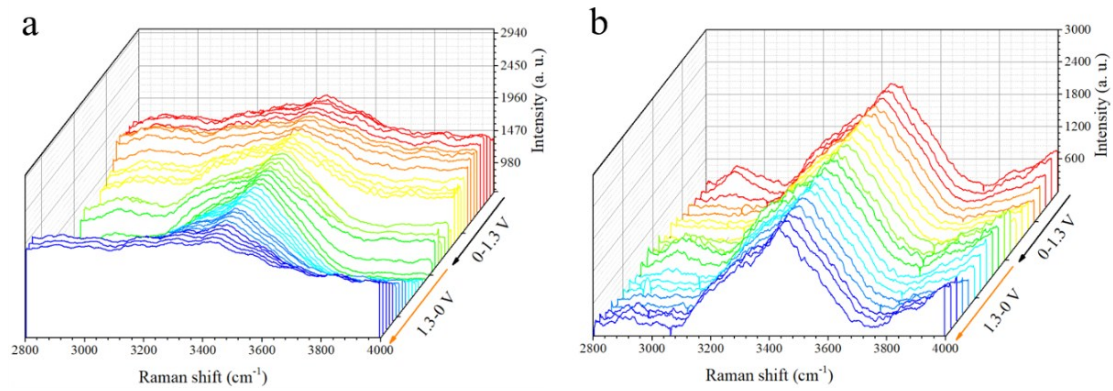
**Figure S10.** Raman spectrum from 100 to 4000  $\text{cm}^{-1}$  of NMO-NDs@NG in the  $\text{Na}_2\text{SO}_4$  electrolyte of pH=9.



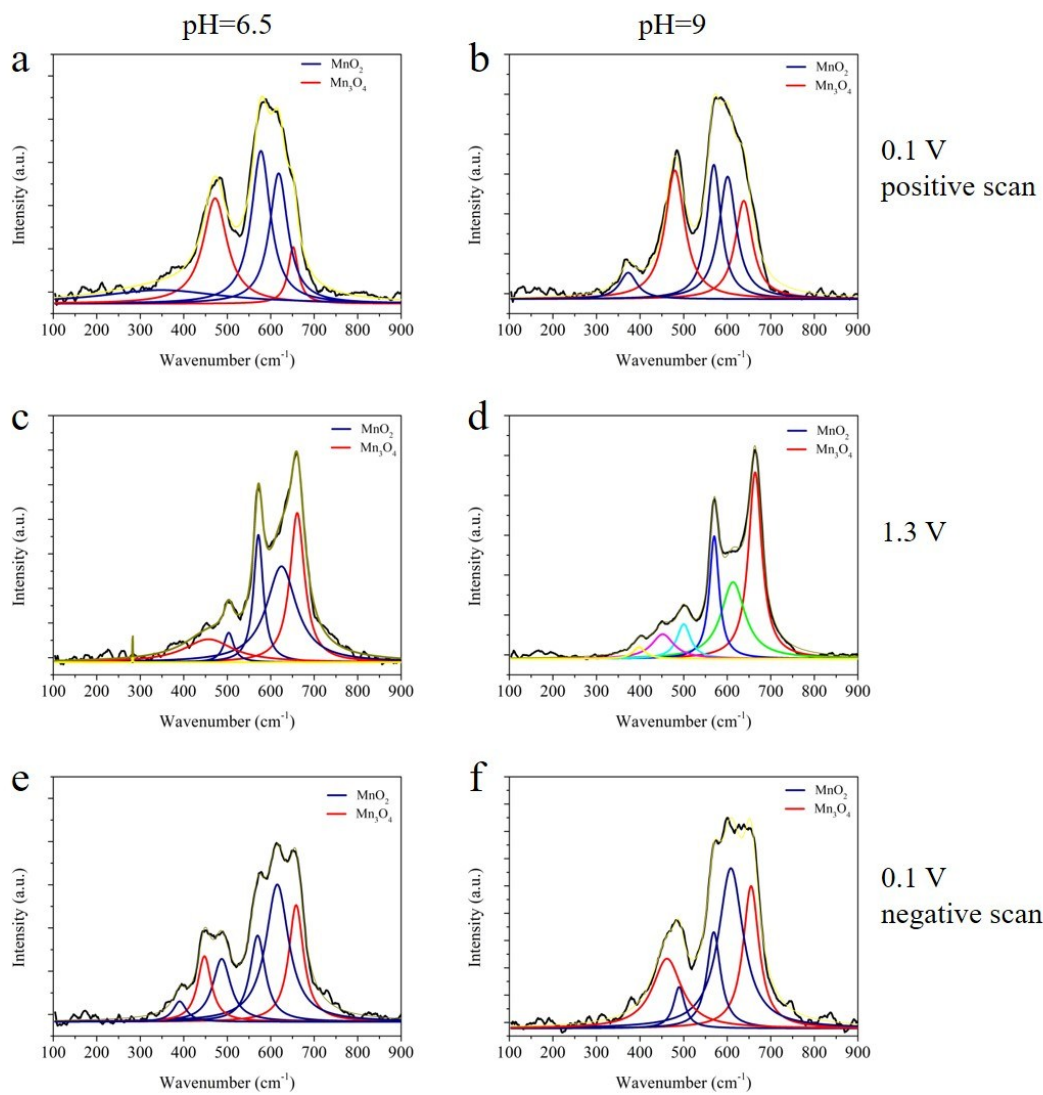
**Figure S11.** Raman spectra of NMO-NDs@NG in the electrolyte of pH=9 (a) and pH=6.5 (b) with the wavenumber from 250 to 1100 cm<sup>-1</sup>.



**Figure S12.** The graphical representation of  $[MnO_6]$  octahedra (a) and the corresponding electron orbitals of  $v_1$  ( $d_z^2$ ) (b) and  $v_2$  ( $d_{x^2-y^2}$ ) (c).<sup>2, 3</sup> Color code: Mn (dark cyan ball); O (yellow ball).

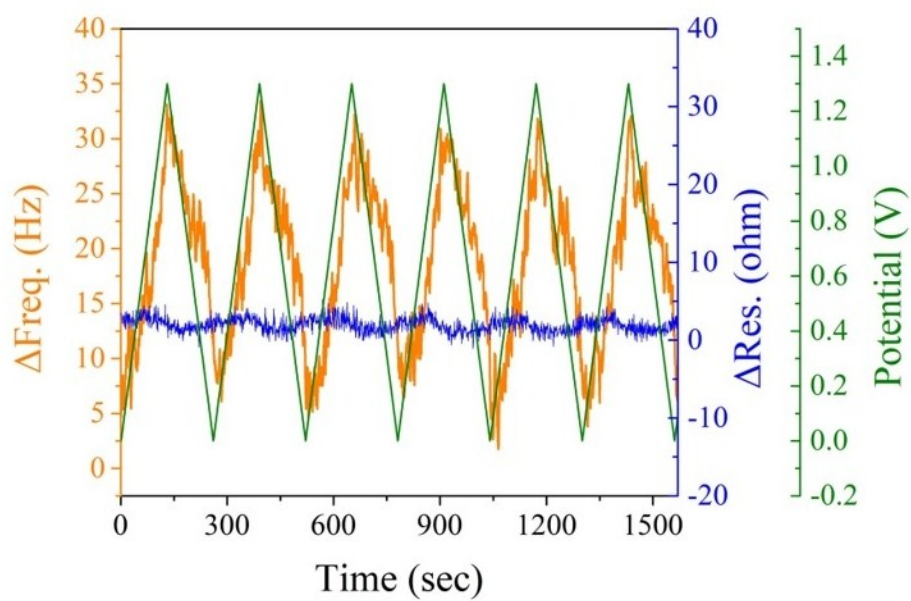


**Figure S13.** The *in-situ* Raman spectrum of the NMO-NDs@NG electrode in the electrolytes of pH=9 (a) and pH=6.5 (b) with the wavenumber from 2800 to 4000  $\text{cm}^{-1}$ .

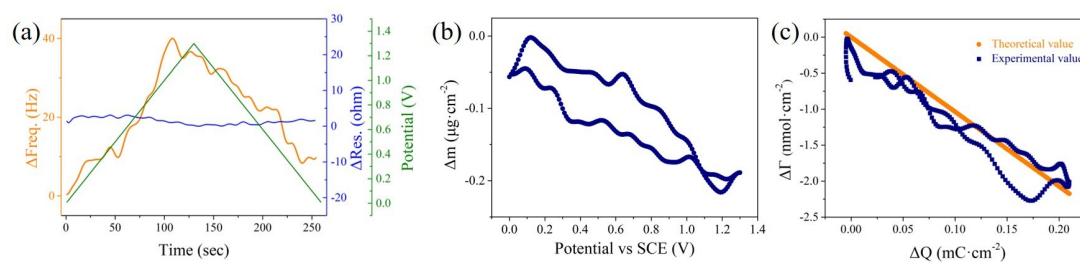


**Figure S14.** Lorentz fitting of in-situ Raman spectrum of NMO-NDs@NG in the electrolytes of pH=6.5 (a, c, e) and in the electrolytes of pH=9 (b, d, f) at the different voltages.

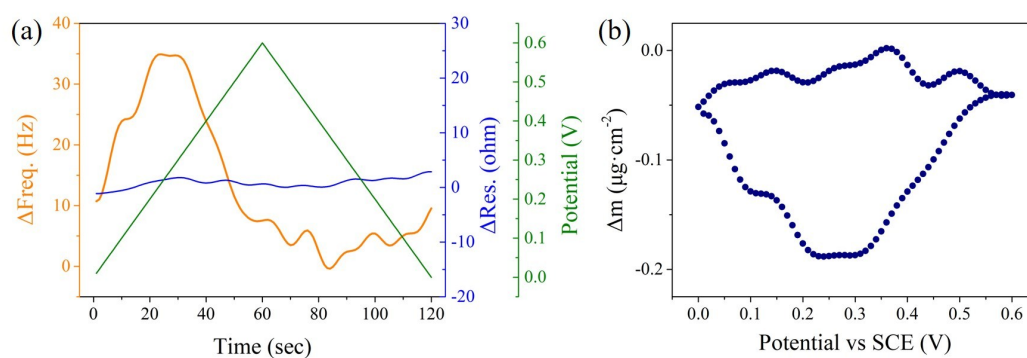




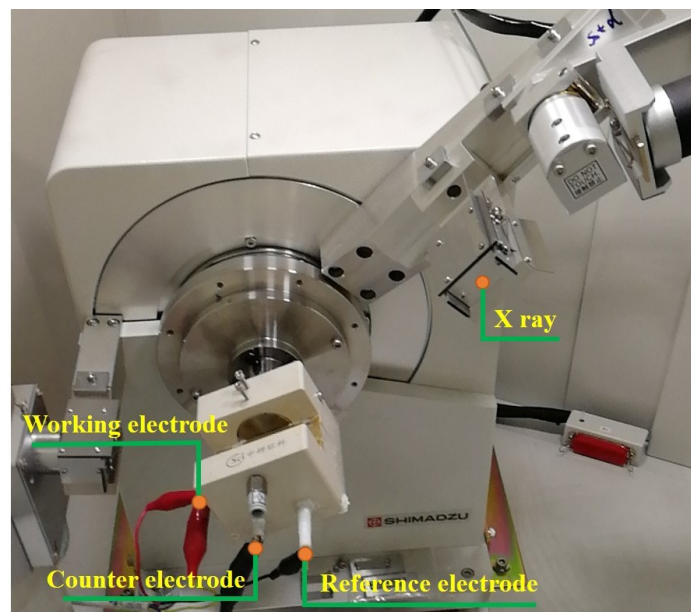
**Figure S15.** Raw EQCM data of NMO-NDs@NG-coated quartz electrodes prepared by VFT technique.



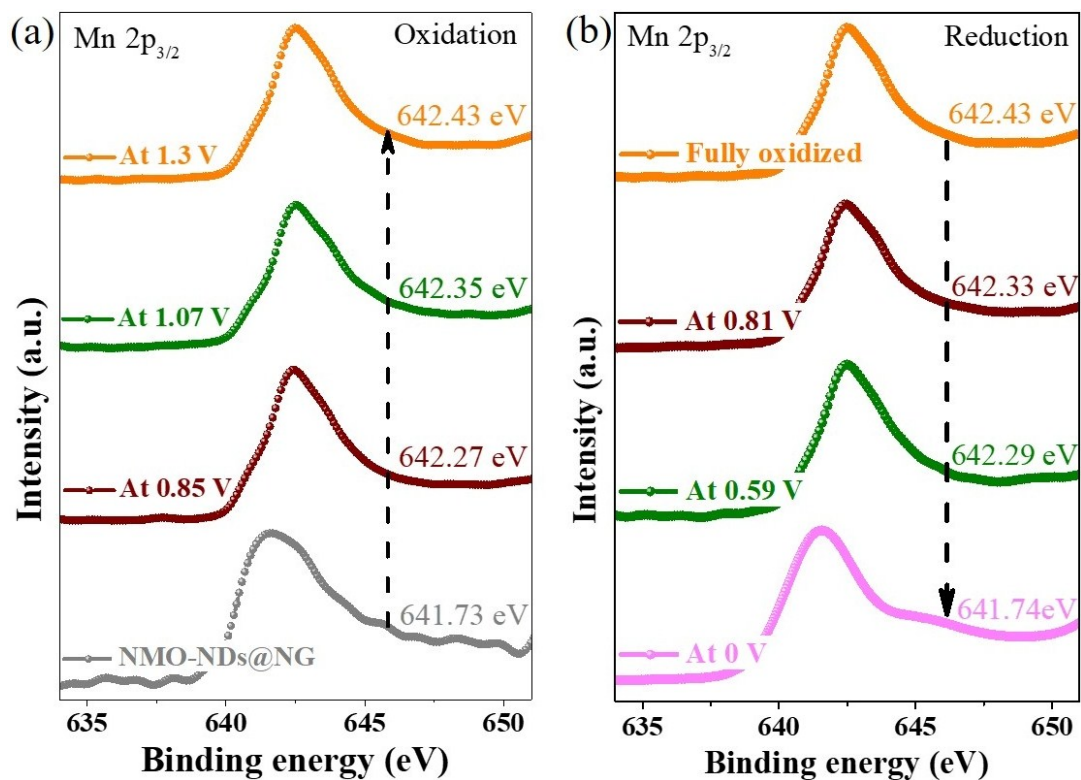
**Figure S16.** EQCM analyze of NMO-NDs@NG in the electrolyte of pH=6.5. (a)  $\Delta\text{Freq.}$ ,  $\Delta\text{Res.}$  and the potential change as function of time during the charge-discharge cycle. (b)  $\Delta m$  as a function of potential. (c) The theoretical and experimental ion population changes ( $\Delta\Gamma$ ) as a function of  $\Delta Q$  during charging and discharging process for the NMO-NDs@NG electrode.



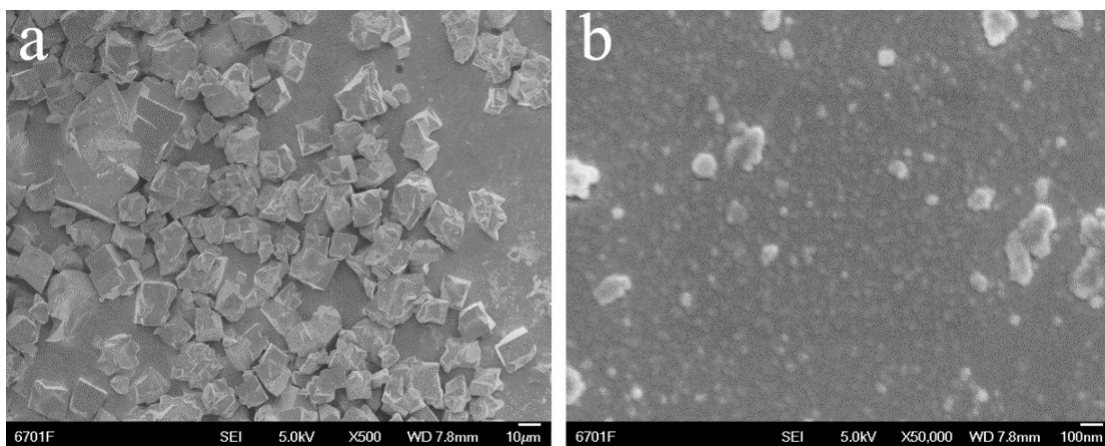
**Figure S17.** EQCM analyze of NMO-NDs@NG in KOH electrolyte. (a)  $\Delta Freq.$ ,  $\Delta Res.$  and the potential change as function of time during the charge-discharge cycle. (b)  $\Delta m$  as a function of potential.



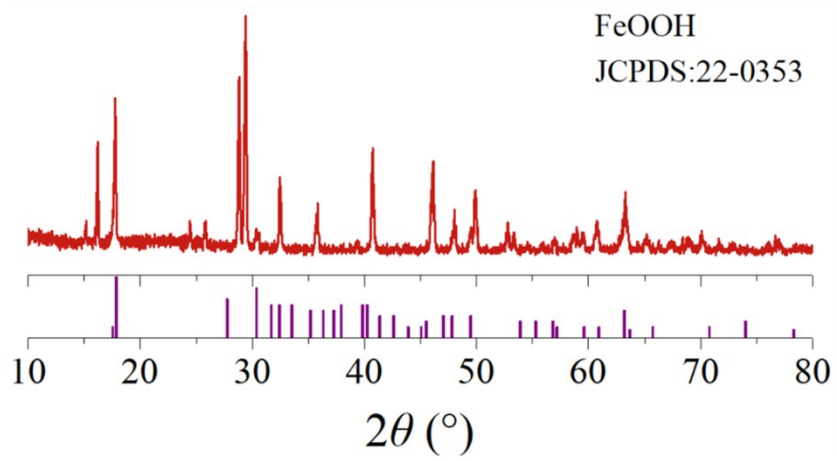
**Figure S18.** The three-electrodes configuration for the in-situ XRD test.



**Figure S19.** Mn 2p<sub>3/2</sub> core-level XPS spectra of the NMO-NDs@NG electrode at different charge (a) and discharge (b) states.

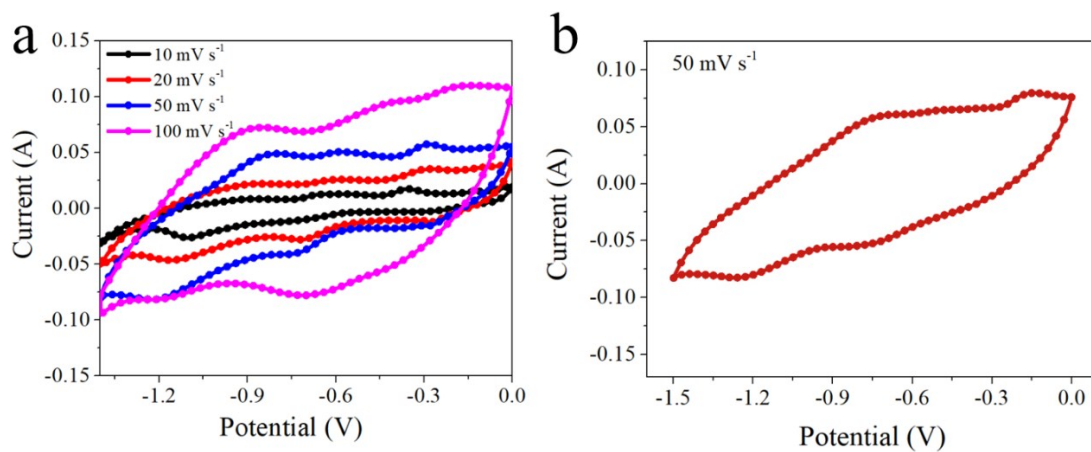


**Figure S20.** SEM images of FeOOH with scale size of 10  $\mu\text{m}$  (a) and 100 nm (b).

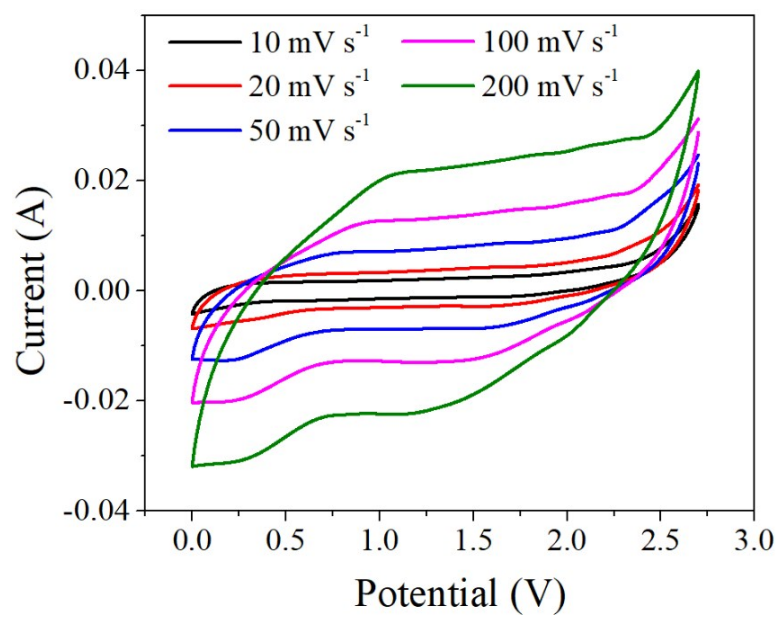


**Figure S21.** XRD pattern of FeOOH.



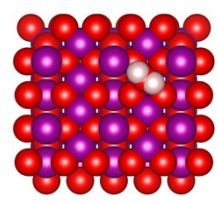
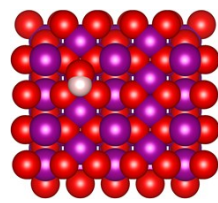
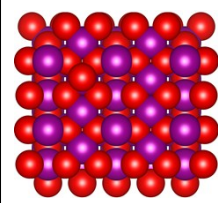
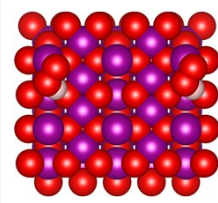
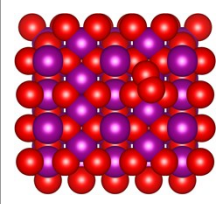


**Figure S22.** CV curves of FeOOH in the electrolyte of pH=9 with a voltage window of -1.4-0 V (a) and -1.5-0 V (b).



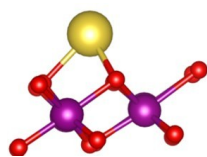
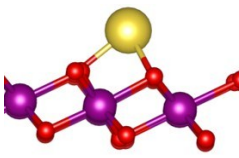
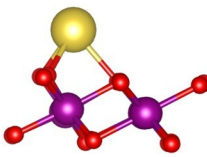
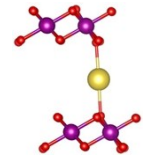
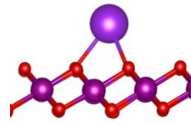
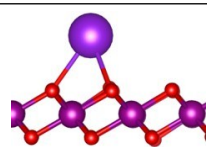
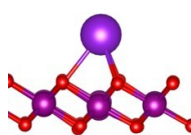
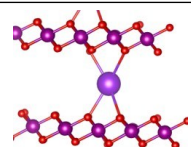
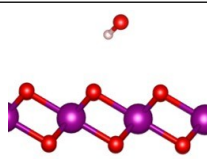
**Figure S23.** CV curves of NMO-NDs@NG//FeOOH hybrid SC in the neutral Na<sub>2</sub>SO<sub>4</sub> electrolyte (pH=6.5) at scan rates from 10 to 200 mV s<sup>-1</sup>.

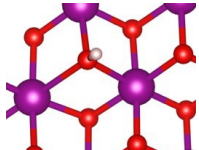
**Table S1.** Free energies at zero potential and the intermediate structures of the OER on O\*-covered NMO(100) surface, obtained by DFT calculations.

				
+2H <sub>2</sub> O(l)	+H <sub>2</sub> O(l)+1/2H <sub>2</sub> (g)	+H <sub>2</sub> O(l)+H <sub>2</sub> (g)	+3/2H <sub>2</sub> (g)	+O <sub>2</sub> +2H <sub>2</sub> (g)
	ΔE <sub>OH</sub> =0.57 eV	ΔE <sub>O</sub> =2.61 eV	ΔE <sub>HOO</sub> =3.36 eV	
ΔG <sub>water</sub> =0.0 eV	ΔG <sub>OH</sub> =0.92 eV	ΔG <sub>O</sub> =2.66 eV	ΔG <sub>HOO</sub> =3.79 eV	ΔG <sub>O<sub>2</sub></sub> =4.96 eV

Violet spheres represent metal ions, red spheres represent oxygen and white spheres represent hydrogen. DFT binding energies were corrected for zero point energy and change in entropy (at 298 K). The corrections were added to the binding energy and free energies of adsorbed O, OH, and OOH, which were 0.05, 0.35, and 0.40 eV, respectively.

**Table S2.** Spin-polarized DFT calculations: the adsorption energy and the bond length of different adsorption configurations.

Configuration	Adsorption energy ( $E_{ads}$ , eV)	Bond length (Å)	Atom model
Na-top	-3.32	2.25	
Na-3fh-O	-2.72	2.23	
Na-3fh-Mn	-3.20	2.26	
Na-middle	-3.87	2.46	
K-top	-4.16	2.68	
K-3fh-O	-4.20	2.70	
K-3fh-Mn	-4.17	2.71	
K-middle	-4.45	3.00	
OH-Mn-top	0.11	3.98	

OH-O-vacancy	-3.77	1.99	
--------------	-------	------	---

## Supplementary Note

### Calculation of average crystallite size:

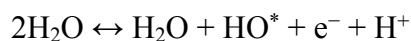
We have calculated the average crystallite size from wide-angle XRD pattern (Figure 1c) for the sample. From the wide-angle XRD pattern, the average crystallite size could be calculated by Debye-Scherrer equation:<sup>4, 5</sup>

$$D = \frac{K\lambda}{\beta \cos \theta}$$

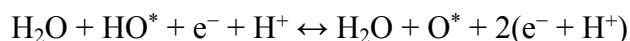
where  $\lambda$  is the X-ray wavelength (0.15405 nm),  $\beta$  is the half height and half width of the diffraction peak (FWHM),  $\theta$  is the diffraction angle,  $K$  is a constant and  $D$  means the average crystallite size. When the FWHM of  $\beta$  is 0.9249,  $\theta$  is 40.66 and  $K$  is 0.9432, the calculated average crystallite size is 9.625 nm.

We have tested the electrochemical performance of NMO-NDs@NG in KOH electrolyte. As shown in Figure S7a, the voltage window of NMO-NDs@NG was 0~0.5 V. And the specific capacity of NMO-NDs@NG was 246 C g<sup>-1</sup> at current density of 1 A g<sup>-1</sup> (Figure S7b). Comparing the energy storage behavior of NMO-NDs@NG in Na<sub>2</sub>SO<sub>4</sub> electrolyte (a surface-controlled pseudocapacitive behavior), NMO-NDs@NG showed a battery-like behavior mainly associated with the reactivity of OH<sup>-</sup> ions in alkaline KOH electrolyte. The results indicated that the charge storage mechanism of NMO-NDs@NG depends largely on the type of electrolytes.

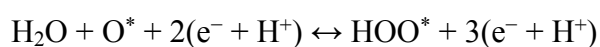
The reactions of water splitting and the corresponding free energies (Figure 4d) can be written as follows:



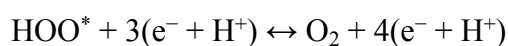
$$\Delta G_1 = \Delta G_{\text{HO}} - \Delta G_{\text{water}}$$



$$\Delta G_2 = \Delta G_{\text{O}} - \Delta G_{\text{HO}}$$



$$\Delta G_3 = \Delta G_{\text{HOO}} - \Delta G_{\text{O}}$$



$$\Delta G_4 = \Delta G_{\text{O}_2} - \Delta G_{\text{HOO}}$$

We have added a full Raman spectrum from 100 to 4000  $\text{cm}^{-1}$  of NMO-NDs@NG in the  $\text{Na}_2\text{SO}_4$  electrolyte of pH=9. As shown in Figure S10, there were three major Raman regions attribute to the Mn-O stretching vibrations of  $[\text{MnO}_6]$  octahedra located at 660-670  $\text{cm}^{-1}$  ( $\nu_1$ ), 569-577  $\text{cm}^{-1}$  ( $\nu_2$ ) and 485-507  $\text{cm}^{-1}$  ( $\nu_3$ ). And the peak located at 980  $\text{cm}^{-1}$  is ascribed to  $\text{SO}_4^{2-}$ . There were two characteristic peaks of D and G peak of NG located at 1300 (D) and 1580 (G)  $\text{cm}^{-1}$ . Because the Raman was tested in aqueous electrolyte of pH=9, there was an obvious O-H stretching vibrations located at 3100-3700  $\text{cm}^{-1}$ .

EQCM measurement can in-situ measure the mass change of an electrode during real-time charging and discharging of the electrode in the presence of difference ions.<sup>6</sup> The



amount of NMO-NDs@NG coated onto the quartz crystal surface is about 40  $\mu\text{g cm}^{-2}$ . The application of EQCM for gravimetric mode implies that the mass change ( $\Delta m$ ) is linked exclusively to the resonant frequency change ( $\Delta Freq.$ ) whereas the simultaneous resonance width change ( $\Delta W$ ) is zero or much smaller than  $\Delta Freq.$ <sup>7, 8</sup> The instrument we used, i.e. Princeton, QCM922A, can measure the resonance resistance change ( $\Delta Res.$ ), which is transformed into the related  $\Delta W$  by the following equation:<sup>9</sup>

$$\Delta W = \frac{16Ae_{26}^2 \rho_q f_q^3}{\pi Z_q^3} \cdot \Delta R$$

where  $e_{26}$  is the piezoelectric stress coefficient ( $9.65 \times 10^{-2} \text{ C m}^{-2}$ ),  $Z_q$  is the acoustic wave impedance ( $8.8 \times 10^6 \text{ kg m}^{-2} \text{ s}^{-1}$ ). Thus, the  $\Delta W$  can be obtained by multiplying the resonance resistance. In our system, the resonance resistance change was about 4  $\Omega$  when the NMO-NDs@NG-coated quartz electrode was cycled between 0 V to 1.3 V (Figure S15). The  $\Delta Freq.$  overwhelmingly prevailed over the  $\Delta W$ , indicating a gravimetric behavior of the quartz-crystal microbalance.

EQCM can measure the  $\Delta Freq.$ , which can be converted to the  $\Delta m$  by Sauerbrey's Equation:<sup>10</sup>

$$\Delta m = - \frac{A \mu_q \rho_q}{2f_q^2} \cdot \Delta f = -C_f \cdot \Delta f$$

where  $A$  is the area of active surface ( $0.198 \text{ cm}^2$ ),  $\mu_q$  is the AT-cut quartz constant ( $2.947 \times 10^{11} \text{ g cm}^{-1} \text{ s}^{-2}$ ),  $\rho_q$  is the quartz crystal density ( $2.65 \text{ g cm}^{-3}$ ),  $f_q$  is the reference frequency (9.00 MHz). Here, the sensitivity factor  $C_f$  is  $5.682 \text{ ng Hz}^{-1} \text{ cm}^{-2}$ .

The experimental ion population change ( $\Delta\Gamma$ ) was calculated by the following equation:

$$\Delta\Gamma = \frac{\Delta m}{M_i}$$

where  $\Delta m$  is the mass change,  $M_i$  is the molecular mass, and for  $\Delta Q < 0$ ,  $M_i = M(\text{Na}^+) = 23 \text{ (g mol}^{-1}\text{)}$ .

The theoretical ion population change ( $\Delta\Gamma_{theor}$ ) was calculated by using Faraday's law:

$$\Delta\Gamma_{theor} = \frac{\Delta Q}{nF}$$

where  $\Delta Q$  is the charge passed through the electrode (C),  $n$  is the valence number of the ion ( $n = 1$ ), and  $F$  is the Faraday constant ( $96485 \text{ C mol}^{-1}$ ).

## Supplementary References

1. H. Kim, J. Hong, K. Y. Park, H. Kim, S. W. Kim and K. Kang, *Chem. Rev.*, 2014, **114**, 11788-11827.
2. L. Y. Liu, L. J. Su, Y. L. Lu, Q. N. Zhang, L. Zhang, S. L. Lei, S. Q. Shi, M. D. Levi and X. B. Yan, *Adv. Funct. Mater.*, 2019, **29**, 12.
3. Q. N. Zhang, M. D. Levi, Q. Y. Dou, Y. L. Lu, Y. G. Chai, S. L. Lei, H. X. Ji, B. Liu, X. D. Bu, P. J. Ma and X. B. Yan, *Adv. Energy Mater.*, 2019, **9**, 10.
4. U. Holzwarth and N. Gibson, *Nat. Nanotechnol.*, 2011, **6**, 534-534.
5. P. Thompson, D. E. Cox and J. B. Hastings, *J. Appl. Crystallogr.*, 1987, **20**, 79-83.
6. Q. Zhang, M. D. Levi, Y. Chai, X. Zhang, D. Xiao, Q. Dou, P. Ma, H. Ji and X. Yan, *Small Methods*, 2019, **3**, 1900246.
7. M. D. Levi, S. Sigalov, D. Aurbach and L. Daikhin, *J. Phys. Chem. C*, 2013, **117**, 14876-14889.
8. M. D. Levi, N. Shpigel, S. Sigalov, V. Dargel, L. Daikhin and D. Aurbach, *Electrochim. Acta*, 2017, **232**, 271-284.
9. Johannsmann and Diethelm, *The quartz crystal microbalance in soft matter research*. (Springer, 2015), 10.1007/978-3-319-07836-6, 343-358.
10. M. Hepel, In *Interfacial Electrochemistry: Theory: Experiment, and Applications*, Wieckowski, A., Ed., Marcel Dekker, Inc.: New York, 1999.